Electronic Supplementary Information

Two-Dimensional MoS_2-Melamine Hybrid Nanostructures for Enhanced Catalytic Hydrogen Evolution Reaction

In Hye Kwak,[‡a] Ik Seon Kwon,[‡a] Tekalign Terfa Debela[‡b] Jaemin Seo,[a] Jae-Pyoung Ahn,[c] Seung Jo Yoo,[d] Jin-Gyu Kim,[d] and Jeunghee Park*[a] and Hong Seok Kang*[e]

[a] Department of Chemistry, Korea University, Sejong 339-700, Republic of Korea; E-mail address: parkjh@korea.ac.kr

[b] Institute for Application of Advanced Materials, Jeonju University, Chonju, Chonbuk 55069, Republic of Korea.

[c]Advanced Analysis Center, Korea Institute of Science and Technology, Seoul 136-791, Republic of Korea.

[d] Division of Electron Microscopic Research, Korea Basic Science Institute, Daejeon 305-806, Republic of Korea.

[e] Department of Nano and Advanced Materials, College of Engineering, Jeonju University, Chonju, Chonbuk 55069, Republic of Korea; E-mail address: hsk@jj.ac.kr

‡I. H. Kwak, I. S. Kwon, and T. T. Debela equally contribute as the first author.

Contents

I. Experimental Section

II. Supplementary Tables

Table S1. Fitted parameters of EXAFS data.

Table S2. Impedance parameters from Nyquist plot.

Table S3. Comparison of HER performance (Tafel parameters and TOF) with other works.

III. Supplementary Figures

Fig. S1 SEM and TEM images of MoS_2-Me-10% and MoS_2-Me-14%.

Fig S2. TEM, STEM, and EDX mapping data of MoS_2-Me.

Fig. S3 XRD pattern of melamine and crystal structures.

Fig. S4 SEM and TEM images of m-melamine and o-melamine powders.

Fig. S5 NMR spectra.

Fig. S6 IR and Raman spectra.

Fig. S7 XANES and FT EXAFS data.

Fig. S8 XPS survey and fine-scanned spectrum.

Fig. S9 TEM and EDX data of MoS_2-Me-10% after 10 h HER.

Fig. S10 XPS data of MoS_2-Me-10% before/after 10h HER.

Fig. S11 TEM, XRD, and XPS spectrum of MoS_2/o-Me and MoS_2/g-C_3N_4 mixture.

Fig. S12 HER performance of MoS_2/o-Me and MoS_2/*g*-C_3N_4 mixture.

Fig. S13 Nyquist plots.

Fig. S14 Cyclic voltammograms for evaluation of double-layer capacitance.

Fig. S15 Structure (6×6) MoS_2-MeH-3 in top and side views showing two possible conformations of MeH molecules.

Fig. S16 $\Delta q(z)$ and $\Delta Q(z)$ versus z for (6×6) MoS_2-MeH-9.

Fig. S17 Structures of (6×6) $2MoS_2$-MeH-3 in slab geometry: various adsorption sites of H atoms are shown in Volmer reaction.

IV. References

I. Experimental Section

Characterization. The products were characterized by field-emission transmission electron microscopy (FE TEM, FEI TECNAI G2 200 kV, Jeol JEM 2100F, HVEM). Energy-dispersive X-ray fluorescence spectroscopy (EDX) with elemental maps was measured using a TEM (FEI Talos F200X) operated at 200 kV that equipped with high-brightness Schottky field emission electron source (X-FEG) and Super-X EDS detector system (Bruker Super-X). This EDX has powerful sensitivity and resolution in the low photon energy region. Fast Fourier-transform (FFT) images were generated by the inversion of the TEM images using Digital Micrograph GMS1.4 software (Gatan Inc.).

High-resolution X-ray diffraction (XRD) patterns were obtained using the 9B and 3D beamlines of the Pohang Light Source (PLS) with monochromatic radiation (λ = 1.54595 Å). XRD pattern measurements were also carried out in a Rigaku D/MAX-2500 V/PC using Cu K_α radiation (λ = 1.54056 Å). X-ray photoelectron spectroscopy (XPS) measurements were performed using the 8A1 beam line of the PLS, as well as a laboratory-based spectrometer (Thermo Scientific Theta Probe) using a photon energy of 1486.6 eV (Al Kα). X-ray absorption near edge spectra (XANES) and extended X-ray absorption fine structure (EXAFS) spectra at the Mo K-edge were collected in transmission mode using the 10C beam line of the PLS with a ring current of 350 mA at 3.0 GeV. Energy calibration was carried out by simultaneously measuring the reference spectrum of Mo metal foil. Least-squares fits of EXAFS data were performed using the Athena and Artemis software packages, version 0.9.25.

The solid-state ^{13}C (100.64 MHz) NMR spectra were acquired on a Bruker AVANCE II$^+$ 400 MHz NMR system (at the KBSI Seoul Western Center) equipped with a Bruker 3.2 mm bore

HXY probe operating in HX mode. The magic angle spinning ^{13}C NMR experiments (one pulse method) were performed using a pulse length of 2 μs for a π/2 pulse length of 5 μs, and a pulse repetition delay time of 3 s. The spectra were referenced to an external adamantane standard in which the peak at higher chemical shift was set at 38.43 ppm. The spectra were processed using the Bruker Topspin software (version 3.2) using conventional techniques, and a 50 Hz line broadening window function was applied in all cases.

Attenuated total reflectance Fourier transform infrared (ATR FTIR) spectra were obtained on a LabRam ARAMIS IR^2 (HORIBA JOBIN YVON). Spectra were collected by pressing the sample onto a diamond crystal with a pressure setting of 90 on the DuraScope. Each spectrum consisted of 16 spectra co-added accumulated between 4000 cm^{-1} and 560 cm^{-1} with a spectral resolution of 4 cm^{-1}. Raman spectra were measured with a micro-Raman spectrometer (Horiba ARAMIS IR2), using a diode laser with an excitation wavelength of 532 nm.

Electrochemical Measurements. Experiments were carried in a three-electrode cell connected to an electrochemical analyzer (CompactStat, Ivium Technologies). HER electrocatalysis (in 0.5 M H_2SO_4 electrolyte) was measured using a linear sweeping from 0 to -0.8 V (vs. RHE) with a scan rate of 2 mV s^{-1}. A saturated calomel electrode (SCE, KCl saturated, Basi Model RE-2BP) was used as reference electrode, and a graphite rod (6 mm dia. × 102 mm long, 99.9995%, Alfa Aesar) was used as counter electrode. The electrolyte was purged with H_2 (ultrahigh grade purity) during the measurement. The applied potentials (E) reported in our work were referenced to the reversible hydrogen electrode (RHE) through standard calibration. In 0.5 M H_2SO_4 electrolyte (pH 0), E (vs. RHE) = E (vs. SCE) + E_{SCE} (= 0.241 V) + 0.0592 pH = E (vs. SCE) + 0.241 V. The overpotential (η) was defined as E (vs. RHE). 4 mg MoS_2 sample was mixed with 1 mg carbon black (Vulcan XC-72) dispersed in Nafion (20 μL) and isopropyl

alcohol (0.98 mL). The catalyst materials (0.39 mg cm^{-2}) were deposited on a glassy carbon rotating disk electrode (RDE, area = 0.1641 cm^2, Pine Instrument),), and a rotation speed of 1600 rpm was used for the linear sweep voltammetry (LSV) measurements. The Pt/C (20 wt.% Pt in Vulcan carbon black, Sigma-Aldrich) tested as reference sample using the same procedure.

Electrochemical impedance spectroscopy (EIS) measurements were carried out for the electrode in an electrolyte by applying an AC voltage of 10 mV in the frequency range of 100 kHz to 0.1 Hz at a bias voltage of -0.15 V (vs. RHE). To measure double-layer capacitance via CV, a potential range in which no apparent Faradaic processes occur was determined from static CV. This range is 0.1–0.2 V. All measured current in this non-Faradaic potential region is assumed to be due to double-layer capacitance. The charging current, i_c, is then measured from CVs at multiple scan rates. The working electrode was held at each potential vertex for 10 s before beginning the next sweep. The charging current density (i_c) is equal to the product of the scan rate (ν) and the electrochemical double-layer capacitance (C_{dl}), as given by equation $i_c = \nu C_{dl}$. The difference ($\Delta J_{0.15}$) between the anodic charging and cathodic discharging currents measured at 0.15 V (vs. RHE) was used for i_c. Thus, a plot of $\Delta J_{0.15}$ as a function of ν yields a straight line with a slope equal to $2 \times C_{dl}$. The scan rates were 20–100 mV s^{-1}.

TOF Calculation. The active site density and per-site turnover frequency (TOF) have been estimated as follows. It should be emphasized that since the nature of the active sites of the catalyst is not clearly understood yet and the real surface area for the nanostructured heterogeneous catalyst is hard to accurately determine, the following result is really just an estimation.

To estimate the active surface site density, we used the C_{dl} value, and further calculate the electrochemically active surface area. The roughness factor (basically the surface area ratio between the catalyst vs. the metal electrodes (0.035 mF cm^{-2}), [S1] for example, is 33.6 mF cm^{-2}/0.035 mF cm^{-2} = 960.

The number of catalytic sites on the surface of flat catalyst can be calculated based on the crystal structure of distorted octahedral-phase 1T' MoS_2. Using the lattice parameters of 1T' phase MoS_2 (we calculated as a = 3.18 Å, b = 3.26 Å, γ = 119°) and assuming one active site per MoS_2 (which translates into on reactive sites per unit cell), the density of surface active sites is: $1/(0.5 \times 3.18 \times 3.26 \times \sin 119°) \times 10^{16}$ cm^{-2} = 2.2×10^{15} atom cm^{-2}).[S2] Our DFT calculation shows that the S atoms below the one NH_2 group of Me are most active sites. So the number of surface active sites was calculated as $0.04 \times 2.2 \times 10^{15}$ atom cm^{-2} = 8.8×10^{13} atom cm^{-2} for MoS_2-Me-10% with $[Me]_I$ = 4%. The density of surface active sites (m) on geometric area: 8.8×10^{13} atom cm^{-2} × 960 (= roughness factor) = 8.45×10^{16} atom cm^{-2}.

The total number of hydrogen (H_2) gas turns overs was calculated from the current density (J in mA cm^{-2}) according to n_{H2} = J (mA cm^{-2})/1000 mA × 1 C s^{-1} × 1 mol e^-/96486 C × (1 mol H_2/2 mol e^{-1}) × (6.022×10^{23} H_2 molecules/1 mol H_2) = 3.12×10^{15} H_2 s^{-1} cm^{-2} per mA cm^{-2}.

For MoS_2-Me-10% ($[Me]_I$ = 4%), the per-site TOF at η = 0.2 V (with a current density of 247.6 mA cm^{-2}) is n_{H2}/m (=density of surface active sites) = $247.6 \times 3.12 \times 10^{15}$ H_2 s^{-1} cm^{-2} / 8.45×10^{16} atom cm^{-2} = 9.1 H_2 s^{-1}.

II. Supplementary Tables

Table S1. Fitting parameters of EXAFS data (**Fig. 2** and **Fig. S6**) for the MoS_2 samples.

Sample	Scattering Path	R (Å)[a]	CN[b]	ΔE (eV)[c]	σ^2 (Å^2)[d]
MoS_2	Mo-S	2.40	6.2 ± 0.3	1.3	0.0028
	Mo-Mo	3.16	4.2 ± 0.8	0.8	0.0036
MoS_2-Me-5%	Mo-S	2.39	4.5 ± 0.7	-1.1	0.0081
	Mo-Mo	2.76	1.4 ± 0.9	2.6	0.0096
MoS_2-Me-7%	Mo-S	2.39	3.8 ± 0.6	-2.3	0.0092
	Mo-Mo	2.75	1.8 ± 0.5	1.2	0.0066
MoS_2-Me-10%	Mo-S	2.37	3.6 ± 0.6	-2.1	0.0072
	Mo-Mo	2.75	1.7 ± 1.2	1.3	0.0086
MoS_2-Me-14%	Mo-S	2.38	3.9 ± 0.8	-1.2	0.0064
	Mo-Mo	2.78	1.8 ± 1.3	1.8	0.0035

[a] Distance between scattering atoms.
[b] Coordination number of Mo atoms.
[c] Edge energy shift, representing between the energy grids of experimental and theoretical data.
[d] Debye-Waller factor, which measure the static and thermal disorder, is three-times larger for the MoS_2-Me samples than MoS_2. It suggests that the intercalation produces a broad range of Mo-S and Mo-Mo distances.

Table S2. Impedance parameters for the equivalent circuit that was shown in **Fig. S8** and **Fig. S10**.

Samples	R_s (Ω)	CPE (mF)	R_{ct} (Ω)
MoS_2	6.4	1.12	850.2
MoS_2-Me-5%	6.4	2.05	142.6
MoS_2-Me-7%	6.3	2.23	104.5
MoS_2-Me-10%	5.9	2.74	37.6
MoS_2-Me-14%	6.0	3.12	61.5
MoS_2 + o-Me 10%	6.7	1.86	256.0

Table S3. Comparison of HER performance (in pH 0) of 1T/1T' phase MoS_2 in the literatures: overpotential (η) at current density of 10 cm^2, Tafel slope, and turn-of-frequency (TOF).

Ref. No.	Materials	Phase	η (mV) at 10 mA cm^{-2}	Tafel slope (mV dec^{-1})	TOF (H_2 s^{-1})
S3	MoS_2 Nanosheets	1T	200	40	N/A
S4	n-BuLi treated MoS_2	1T	187	43	N/A
S5	Ammoniated MoS_2	2H	320	45	N/A
S6	Single layer MoS_2	1T	N/A	45	0.019-0.046 at 0 V
S7	MoS_2 nanosheets	1T	175	41	N/A
S8	MoS_2 monolayer	1T'	300	61	3.8±1.6 at 0.077 V
S9	Functionalized MoS_2 nanosheets	1T	348	75	N/A
S10	Pd doped MoS_2	1T	89	62	16.54 at 0.2 V
S11	MoS_2 /Graphene superlattice	1T	N/A (~140)	48.7	N/A
S12	MoSSe nanodots	1T	140	40	N/A
Present work	MoS_2 – Melamine	1T'	136	37	5.2

III. Supporting Figures

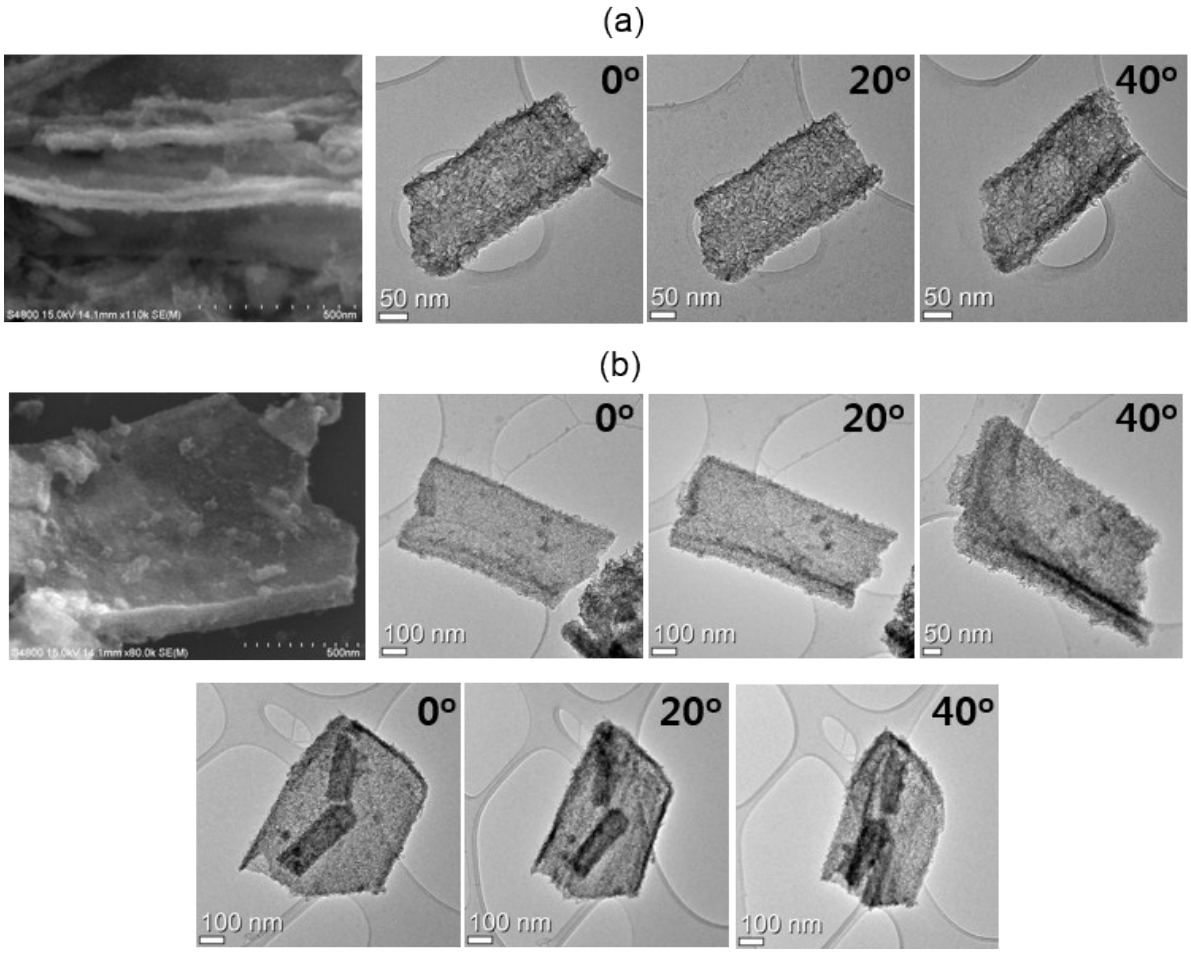

Fig. S1 SEM and HRTEM image of (a) MoS_2-Me-10% and (b) MoS_2-Me-14%.

The SEM image shows the thickness of nanoplates is 40 and 100 nm for MoS_2-Me-7% and (b) MoS_2-Me-14%, respectively. The HRTEM images were measured by tilting the TEM grid holder at angles of 0, 20, and 40 degrees, revealing the lateral side of the nanoplates. The thickness of nanoplates increases from 40 and 100 nm as the [Me] increases from 10% to 14%.

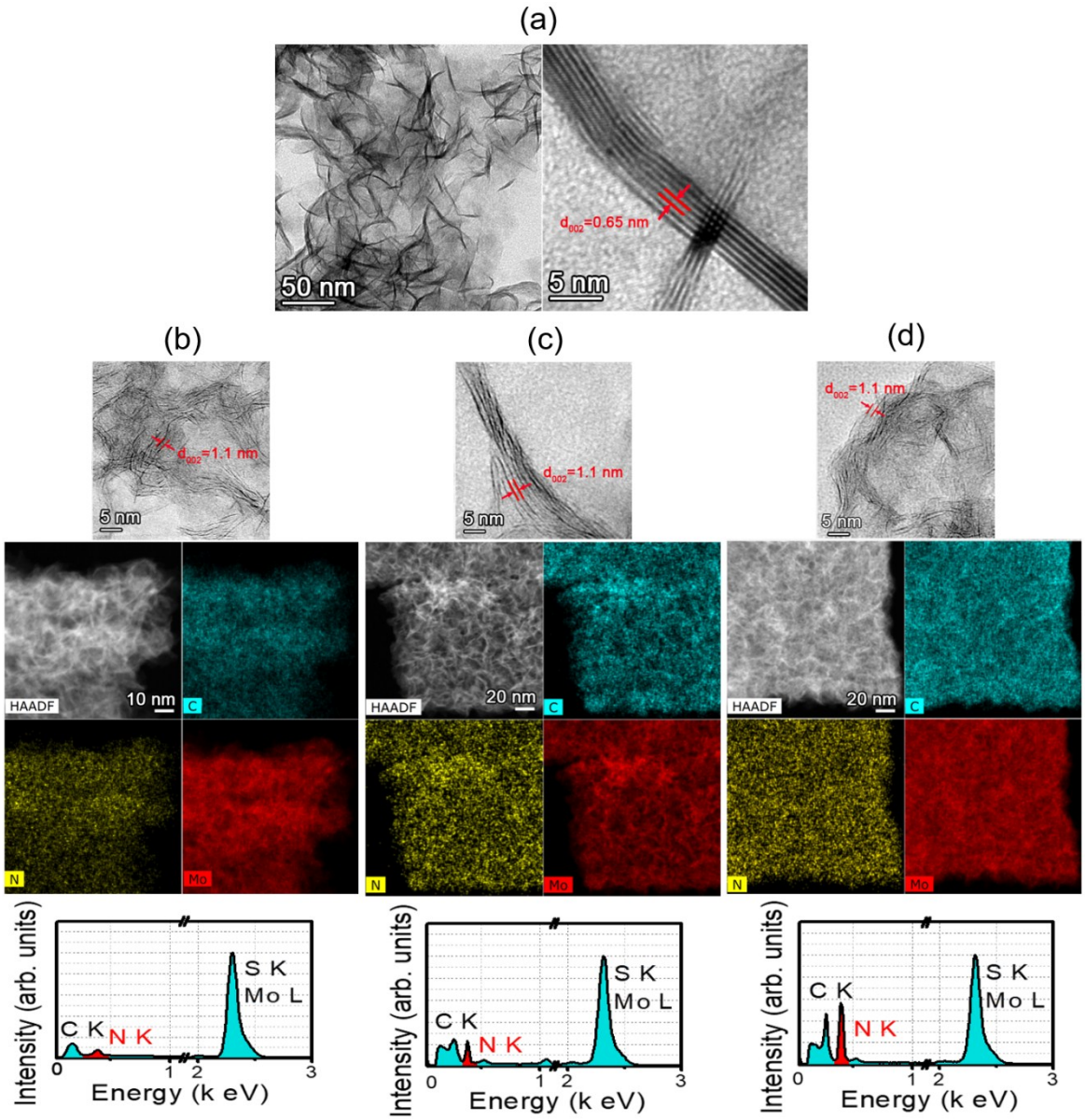

Fig. S2 HRTEM and EDX mapping image of (a) MoS_2, (b) MoS_2-Me-5%, (c) MoS_2-Me-7%, and (d) MoS_2-Me-14%. The lattice-resolved TEM image shows that the average distance between adjacent MoS_2 layers (d_{002}) is 6.5 Å for MoS_2 and 11 Å for all MoS_2-Me samples. The HAADF-STEM image, and EDX elemental mapping and corresponding EDX spectrum shows the homogeneous distribution of C, N, and Mo/S in the entire sample. The intensity of N 1s peak relative to the Mo L-shell (at 2.5 keV) and S K-shell (at 2.4 keV) peaks increases with increasing the concentration of Me.

(a)

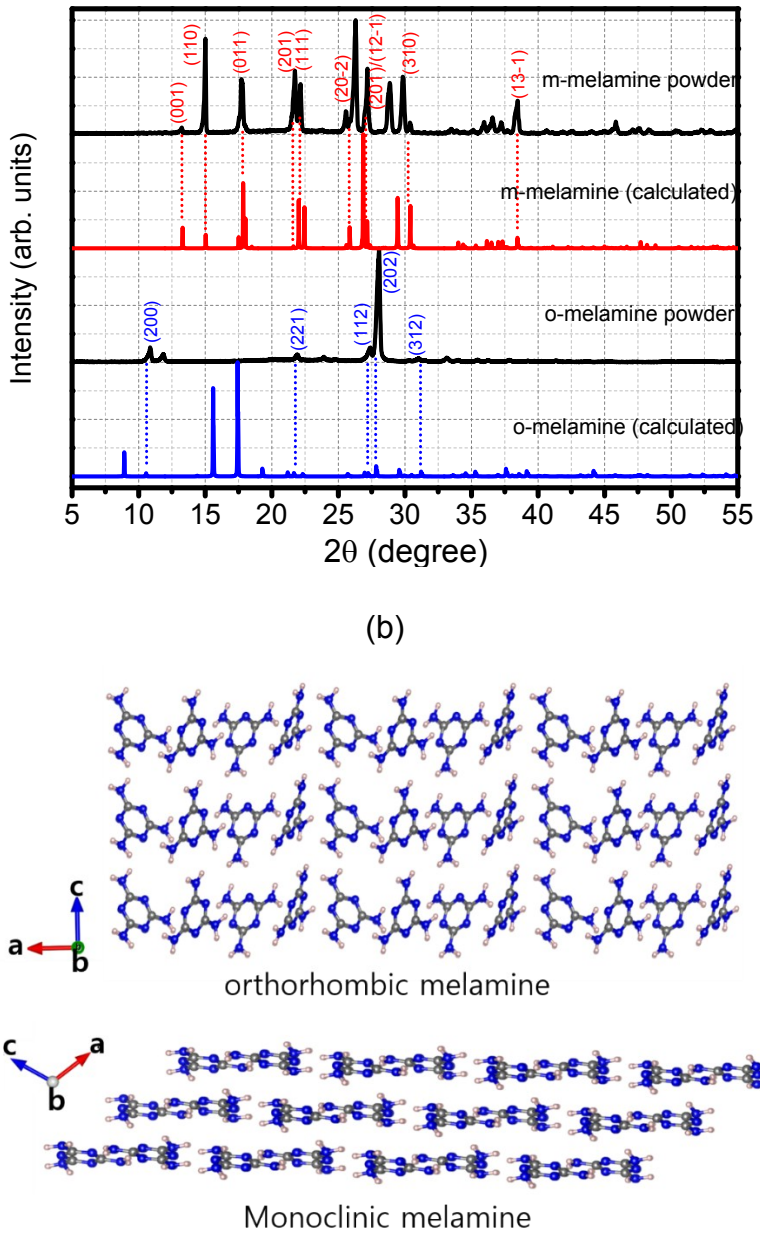

Fig. S3 (a) XRD patterns of orthorhombic phase (o-) melamine (synthesized in this work) and monoclinic phase (m-) melamine powders (purchased from Sigma-Aldrich.). The peaks were referenced to those that calculated one by VESTA program (http://jp-minerals.org/vesta/en/) using the lattice parameters: a = 16.75 Å, b = 12.29 Å, and c = 6.93 Å for orthorhombic phase; a = 10.54 Å, b = 7.45 Å, c = 7.25 Å, and β = 112.2º for monoclinic phase.[S13] (b) Crystal structure of orthorhombic phase melamine and monoclinic phase melamine. The melamine molecules stack along the [001] and [101] direction, for orthorhombic and monoclinic phase, respectively. The XRD pattern of orthorhombic phase (o-) melamine is same as that reported by Tian et al. The peak intensity is very different between the generated and experimental pattern. Nevertheless, the position of some peaks ((200), (221), (112), (202), and (312)) is close to the calculated ones.

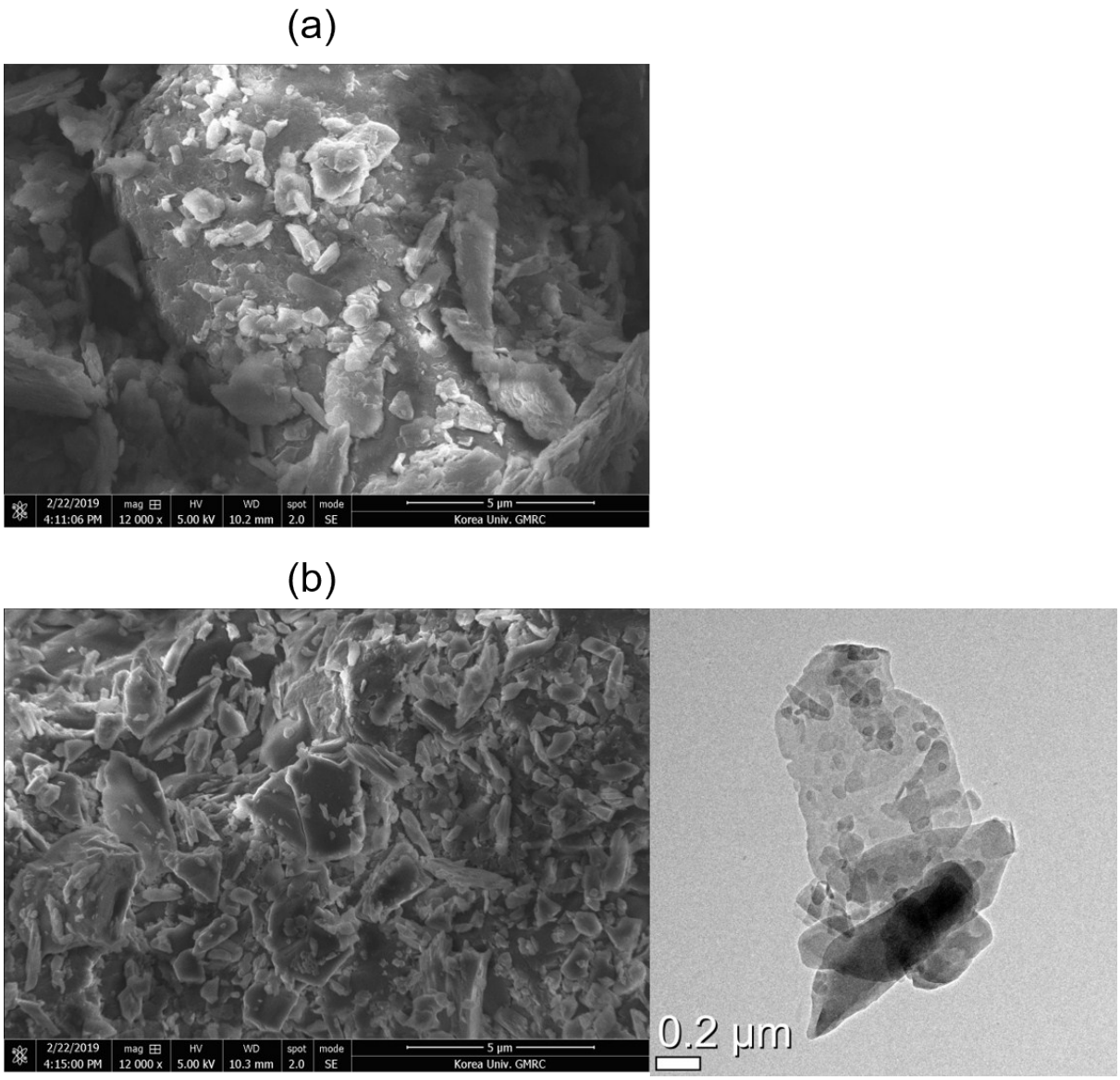

Fig. 4 SEM and TEM images of (a) monoclinic phase Me and (b) orthorhombic phase Me powders. The orthorhombic phase Me powder exhibits more 2D like morphology than monoclinic phase Me powder.

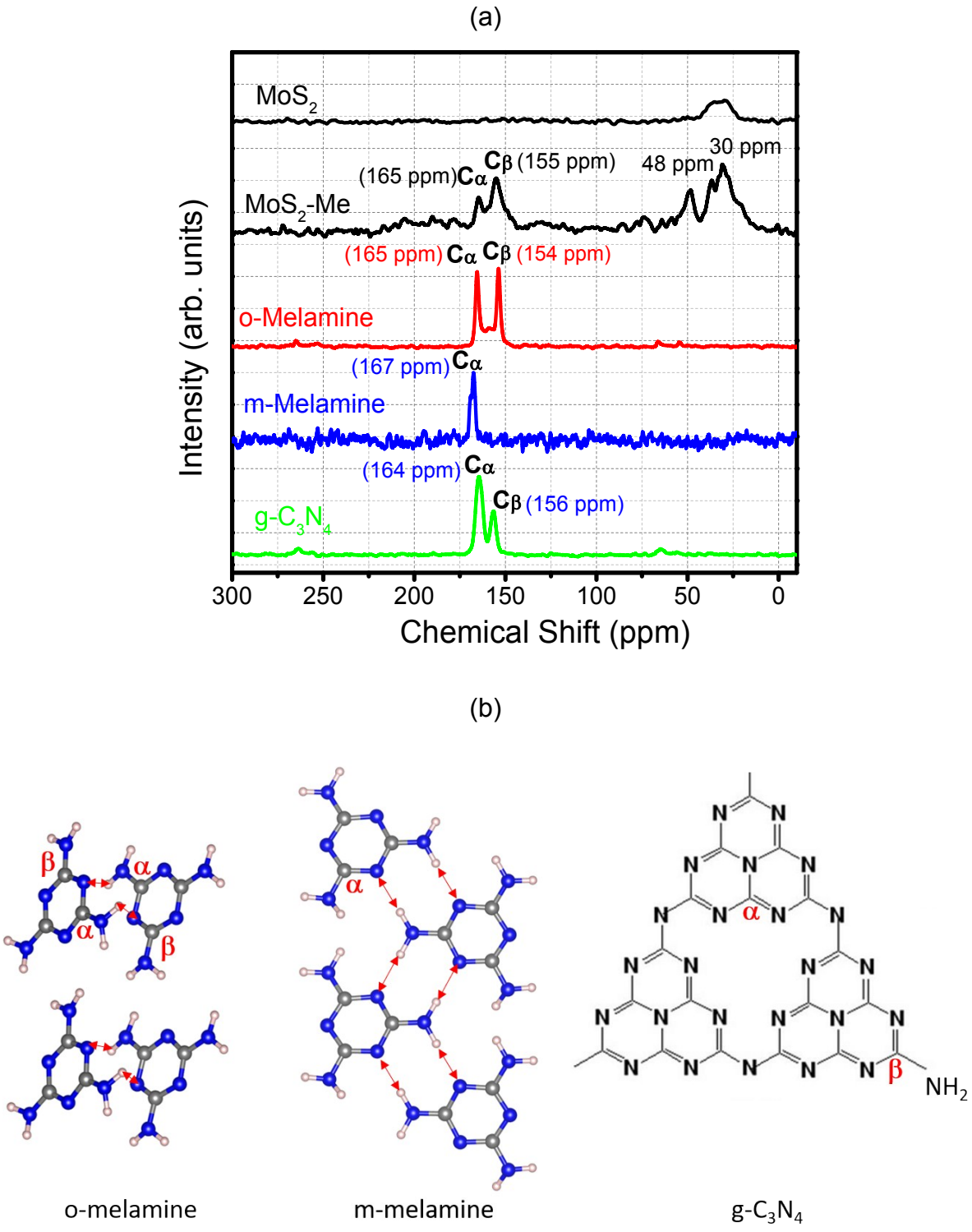

Fig. S5 (a) Solid state ^{13}C NMR spectrum of MoS_2, MoS_2-Me-**10**%, orthorhombic phase (o-) melamine, monoclinic phase (m-) melamine, and *g*-C_3N_4. The m-melamine sample was purchased from Sigma-Aldrich. (b) Top-view crystal structure of o-melamine, m-melamine, and *g*-C_3N_4 that stacked along the [001], [101], and [001] direction, respectively.

The ^{13}C NMR spectrum of o-melamine consisted of two peaks (C_α and C_β) at 165 and 154 ppm, probably originated from the triazine ring. MoS_2-Me-10% shows two peaks at 165 and 155 ppm, whose positions are close to those of o-melamine. The peaks at 48 and 30 ppm can be assigned to the C-N and C-C/C-H that mainly formed by the graphitization during the hydrothermal reaction of melamine, respectively, since the MoS_2 shows much reduced peak at 30 ppm as a background signal.

In order to investigate the origin of those two peaks, the ^{13}C NMR spectrum was further taken for m-melamine and *g*-C_3N_4. The m-melamine crystal shows one triazine ring peak (C_α) at 165 ppm, which is consistent with the previous work.[S15] For bulk g-C_3N_4, the two peaks (C_α and C_β) appear at 164 and 156 ppm.[S14]

In the molecular structure, the C_α and C_β atoms of o-melamine, m-melamine, and *g*-C_3N_4 crystal structures were marked by α and β, respectively. The hydrogen bonds were marked by the arrows. In m-melamine, all N atoms are hydrogen bonded with adjacent melamine molecules, so all C atoms lie in the same hydrogen bonding environment, yielding one C_α peak. For bulk g-C_3N_4, the C_α peak is assigned to the C atoms bonded with three N atoms.[S14] The C_β peak can be originated from the C atoms bonded with the NH_2 end group or defects. In the case of *o*-melamine, two types of C atoms can exist; the C_α atoms attached to the hydrogen bonded NH_2 and the C_β atoms attached to the non-hydrogen bonded NH_2. Therefore, the C_α and C_β peaks of MoS_2-Me-10% are assigned to the C atoms attached to the hydrogen bonded NH_2 and the non-hydrogen bonded NH_2, respectively.

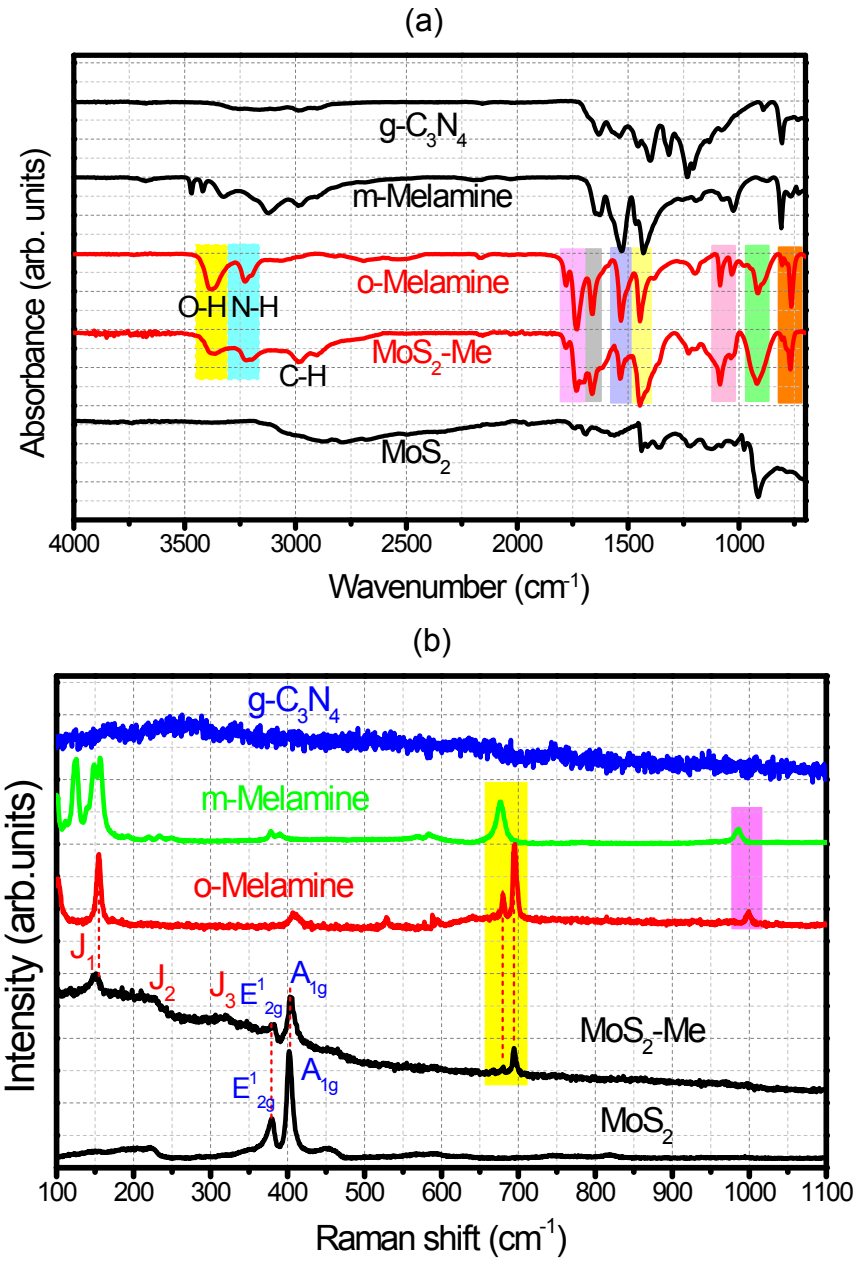

Fig. S6 (a) IR and (b) Raman of MoS_2, MoS_2-Me-10%, orthorhombic phase (o-) melamine, monoclinic phase (m-) melamine, and *g*-C_3N_4. Raman spectrum was obtained by 514 nm Ar ion laser.

IR spectrum of MoS_2-Me-10% and o-melamine show the same feature IR spectrum, which are different from those of m-melamine and g-C_3N_4. This indicates that the o- melamine exists in the MoS_2-Me sample. We assigned the peaks as follows: O-H stretching mode at 3380 cm^{-1} (marked by yellow), N-H stretching mode at 3200 cm^{-1} (marked by light blue), C=O stretching

mode at 1750 cm^{-1} (marked by pink), NH_2 scissoring mode at 1660 cm^{-1} (marked by grey), C-N-C stretching at 1540 cm^{-1} (marked by violet), N-H bending at 1440 cm^{-1} (marked by light yellow), C-OH stretching at 1080 cm^{-1} (marked by light pink), NH_2 wagging stretching at 920 cm^{-1} (marked by light green), and out-of-plane bending od triazine ring at 770 cm^{-1} (marked by light orange). The peaks related with the O-H and C-OH indicate that o-melamine can exist as a hydrate form. The C-H peaks of MoS_2-Me at 3000 cm^{-1} may come from the graphitized form of melamine that produced during the hydrothermal reaction, consistent with the ^{13}C NMR data.

The Raman spectrum of MoS_2-Me exhibits the C-N peaks of *o*-melamine at 695 cm^{-1}. The MoS_2 exhibit two characteristic Raman peaks of the 2H phase at 380 and 403 cm^{-1}, corresponding to the in-plane E^1_{2g} and out-of-plane A_{1g} vibration modes, respectively. The MoS_2-Me also shows the unique Raman peaks of 1T' phase: the J_1 peak at 148 cm^{-1}, the J_2 peak at 236 cm^{-1}, and the J_3 peak at 336 cm^{-1}.[S16] The strong intensity of J_1 peak is due to the peak of o-melamine at 152 cm^{-1}. The Raman speak of m-melamine is different from that of o-melamine, confirming that the MoS_2 and *o*-melamine form a hybrid structure. The Raman peaks of m-melamine are dominated by the two trigonal ring breathing modes, the 675 cm^{-1} mode primarily from C-NH_2 bonds, and the 985 cm^{-1} mode primarily involving the N=C-N.[S17] For o-melamine, we suggest that these two Raman peaks shifted to 690 and 1000 cm^{-1}, respectively. The g-C_3N_4 exhibits no Raman peak, consistently with the previous works.[S18,S19]

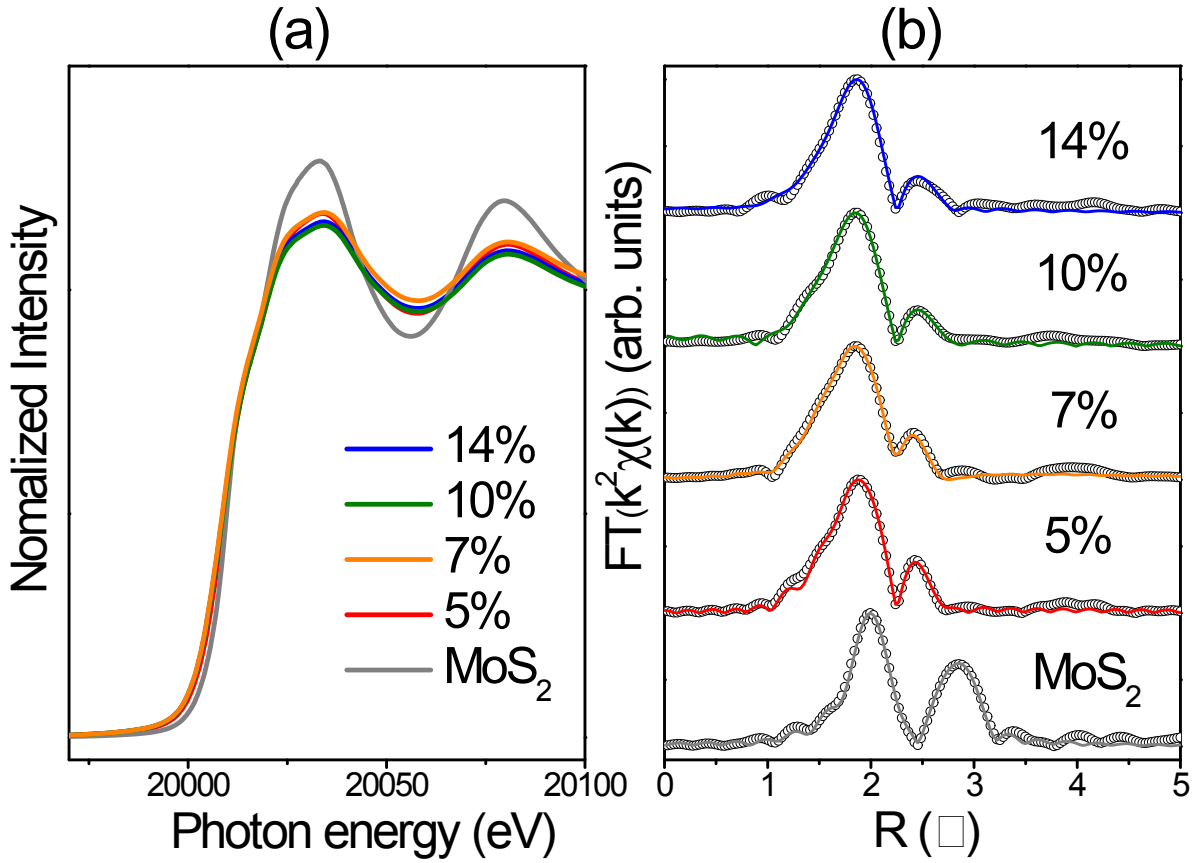

Fig. S7 (a) XANES and (b) FT EXAFS above the Mo K edge for MoS_2 and MoS_2-Me samples (MoS_2-Me-5%, MoS_2-Me-7%, MoS_2-Me-10%, and MoS_2-Me-14%).

(a) X-ray absorption near edge spectra (XANES) above the Mo K-edge shows that the edge energies of all MoS_2-Me are lower than those of MoS_2, due to more metallic 1T' phase MoS_2 than the 2H phase.

(b) Non-phase-corrected, k^2-weighted Fourier-transform extended X-ray absorption fine structure (FT EXAFS) above the Mo K-edge for MoS_2 and MoS_2-Me samples. The FT curves were fitted to Mo–S and Mo–Mo bonds. Table S1 shows the fitting parameters. For 2H phase MoS_2, the distance of Mo–S and Mo–Mo bonds is 2.40 and 3.16 Å, respectively. For MoS_2-Me samples, the distance of Mo–S and Mo–Mo bonds is 2.37-2.39 and 2.75-2.78 Å., respectively.

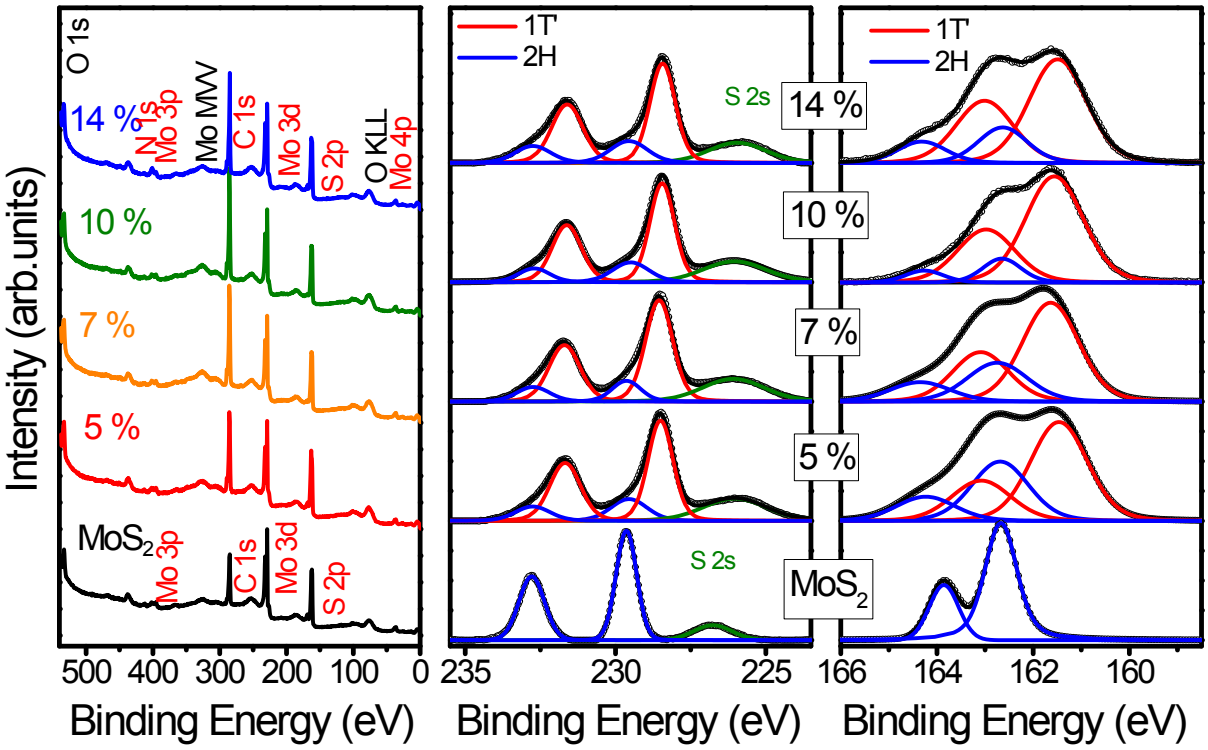

Fig. S8 (a) XPS survey scans, (b) fine-scan Mo 3d, and (c) fine-scan S 2p peaks of MoS_2 and MoS_2-Me samples (MoS_2-Me-5%, MoS_2-Me-7%, MoS_2-Me-10%, and MoS_2-Me-14%). The experimental data (open circles) are fitted by a Voigt function, and the sum of the re solved bands is represented by a black line. The photon energy is 600 eV.

(a) The C peak of MoS_2-Me samples is larger than that of MoS_2, due to the Me molecules.

(b) The 2H phase MoS_2 shows the $3d_{5/2}$ peak at 229.4 eV, which is blue shifted from the Mo metal at 228.0 eV. The peak of MoS_2-Me samples was resolved into the 1T' phase band at 228.8 and the 2H phase band at 229.4 eV. The fraction of 1T' phase was determined to be avg. 80%, indicating that this phase is the major phase.

(c) The S $2p_{3/2}$ and S $2p_{1/2}$ peaks are separated by about 1.2 eV. The MoS_2 shows peaks at 162.1 and 163.3 eV, which are 1.9 eV red-shifted with respect to the signal of neutral S (S^0) at 164.0 and 165.2 eV. They correspond to the S^{2-} anions bonded with the Mo cations in the 2H phase. For the MoS_2-Me samples, the broad peak was resolved into four bands; two each for the 2H phase (blue) and the 1T' phase (red). The larger red-shift bands are assigned to those of electron-rich 1T' phase.

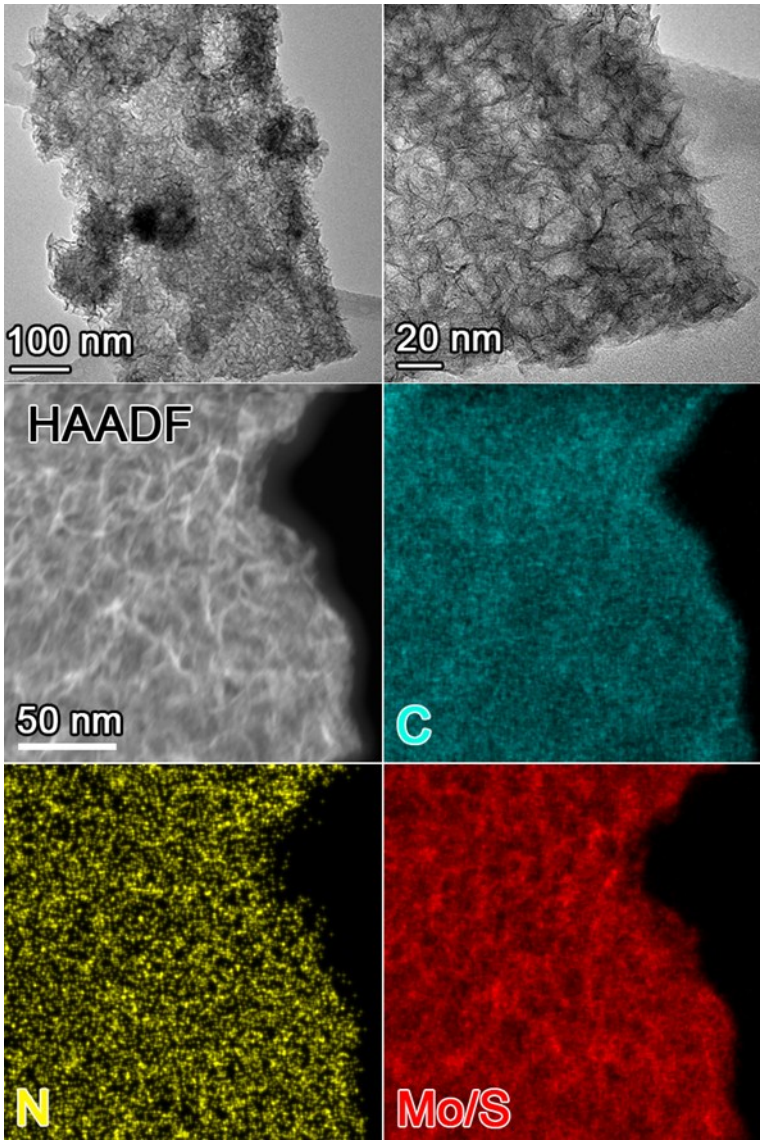

Fig. S9 TEM images, and HADDF image and EDX elemental mappings of MoS_2-Me-10% after 10h HER.

The 2D hybrid nanostructures remains the same after the HER (10 h). The average distance between adjacent MoS_2 layers (d_{002}) is the same as that of the before samples; 11 Å. The EDX mapping and spectrum show that the C, N, and Mo/S atoms distribute homogeneously over the entire samples. The N content remain as 10%.

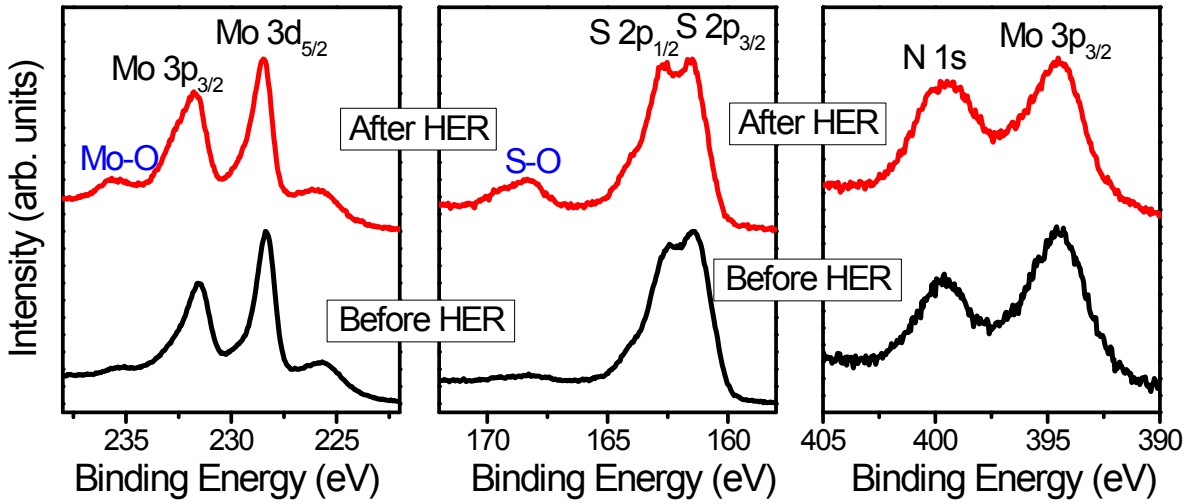

Fig. S10 Fine-scan XPS data of MoS_2-Me-10% after 10h HER; (a) Mo 3d, (b) S 2p, and (c) N 1s and Mo $3p_{3/2}$ peaks.

A laboratory-based spectrometer (Thermo Scientific Theta Probe) using a photon energy of 1486.6 eV (Al Kα) was used, while the XPS shown in Fig. 2 was obtained using the 8A1 beam line of the PLS. The peak profile is somewhat different from that of Fig. 2 and Fig. S4 (ESI). This could be ascribed to the higher photon energy (1486.6 eV vs. 600 eV) and the lower resolution compared to that of the synchrotron radiation. The higher photon energy XPS has a longer penetration depth, so that the peak originated from the Me support becomes dominant. The peak feature of Mo 3d and S 2p, corresponding to the 1T′ phase MoS_2, didn′t change during the HER. The Mo-O and S-O peaks appeared after the HER, probably due to the HER involved on the surface of MoS_2 and the adsorption of electrolyte (0.5M H_2SO_4). The fitting of N 1s peak into the two bands was not possible due to the limit of resolution. Nevertheless, the peak feature of N 1s remains the same after the HER, confirming the stability of the MoS_2-Me hybrid nanostructures.

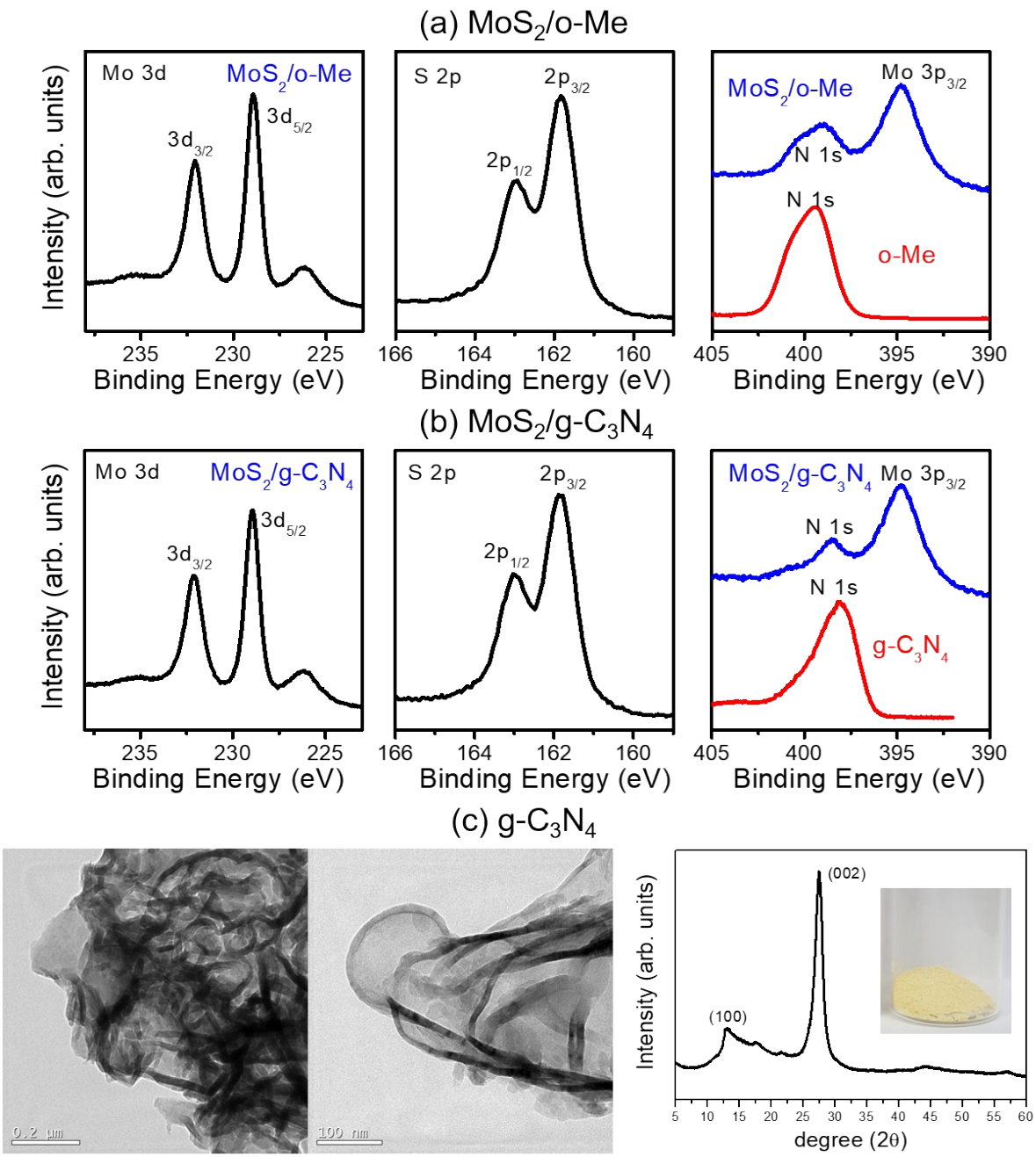

Fig. S11 Fine-scanned XPS Mo 3d, S 2p, and N 1s and Mo $3p_{3/2}$ peaks of (a) MoS_2/o-Me and (b) MoS_2/g-C_3N_4 mixtures. (c) TEM images and XRD pattern of *g*-C_3N_4. Inset corresponds to the photograph showing the yellow g-C_3N_4 nanosheets in a vial.

We prepared a simple mixture of 2H phase MoS_2 nanosheets with o-Me (or *g*-C_3N_4). The TEM images, XRD pattern, and photograph of g-C_3N_4 are shown, consistently with those of the previous works.[S14] A laboratory-based spectrometer (Thermo Scientific Theta Probe) using

a photon energy of 1486.6 eV (Al Kα) was used, while the XPS shown in Figs. 2c and 2d was obtained using the 8A1 beam line of the PLS. Therefore, the peak profiles of 2H phase MoS_2 and o-Me are somewhat different from those shown in Fig. 2. The N 1s peak of o-Me and MoS_2/o-Me appears at 399.5 and 399.2 V, respectively. The N 1s peak of g-C_3N_4 power and MoS_2/g-C_3N_4 mixture appears at 398.2 and 398.5 V, respectively.

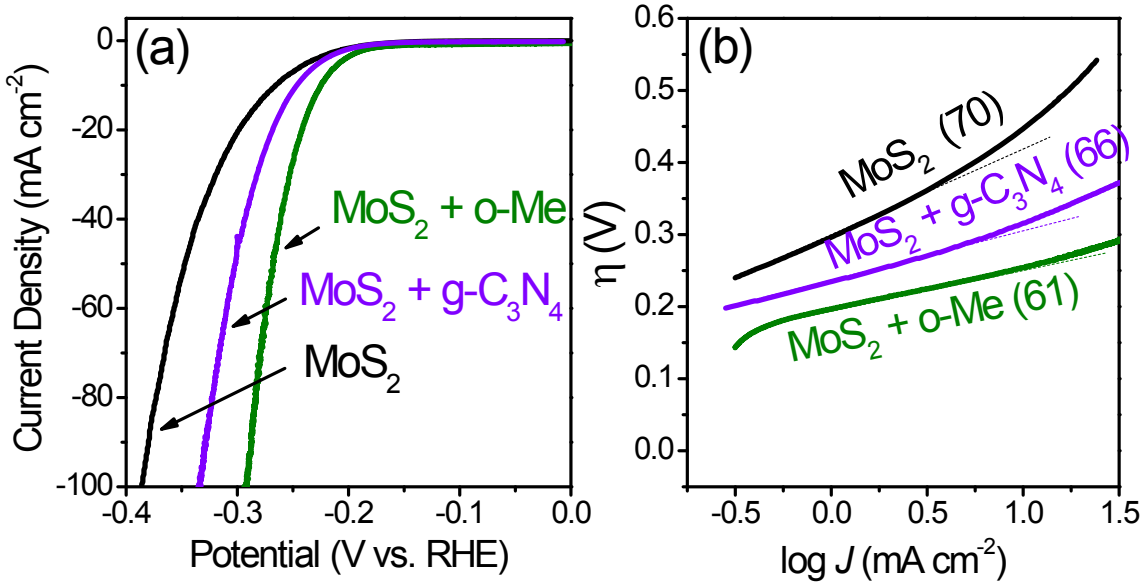

Fig. S12. (a) LSV curves (scan rate: 2 mV s^{-1}) for a mixture of MoS_2, MoS_2/o-Me (with [o-Me]/[MoS_2] 10%) and a mixture of MoS_2/g-C_3N_4 (with [g-C_3N_4]/[MoS_2] = 10%) as catalysts toward HER in H_2-saturated 0.5 M H_2SO_4 (pH 0). (b) Tafel plots derived from the LSV curves in low potential region that corresponds to the activation-controlled region.

The overpotentials (η) required to obtain 10 mA cm^{-2} ($\eta_{J=10}$) is 0.266 V for MoS_2, 0.226 V for MoS_2/o-Me, and 0.246 V for MoS_2/g-C_3N_4, while that of the intercalated MoS_2-Me-10% is 0.136 V. The respective Tafel slope of MoS_2, MoS_2/o-Me, and MoS_2/g-C_3N_4 is 70, 61 and 66 $mVdec^{-1}$, which are larger than that (37 mV dec^{-1}) of the intercalated MoS_2-Me-10%. Therefore, the HER catalytic efficiencies are less than that of MoS_2-Me intercalated samples, indicating that the enhanced efficiency is ascribed to the intercalated Me.

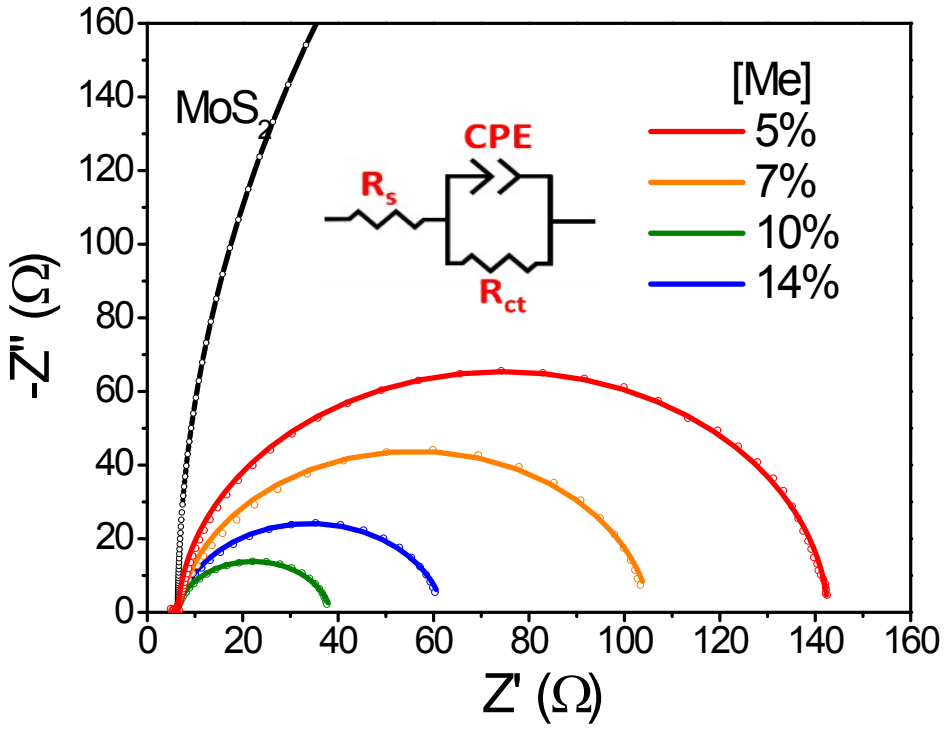

Fig. S13 Nyquist plots for EIS measurements of MoS_2 and MoS_2-Me samples (with [Me] = 0%, 5%, 7%, 10%, and 14%), using the frequency in the range from 100 kHz to 0.1 Hz at a representative potential of -0.15 V (vs. RHE). The modified Randles circuit for fitting is shown in the inset.

Electrochemical impedance spectroscopy (EIS) measurements of the samples were performed using a 100 kHz–0.1 Hz frequency range and an amplitude of 10 mV at η = 0.15 V. In the high-frequency limit and under non-Faradaic conditions, the electrochemical system is approximated by the modified Randles circuit shown in the inset, where R_s denotes the solution resistance, CPE is a constant-phase element related to the double-layer capacitance, and R_{ct} is the charge-transfer resistance from any residual Faradaic processes. A semicircle in the low-frequency region of the Nyquist plots represents the charge transfer process, with the diameter of the semicircle reflecting the charge-transfer resistance. The real (Z') and negative imaginary ($-Z''$) components of the impedance are plotted on the x and y axes, respectively. The simulation of the EIS spectra using an equivalent circuit model allowed us to determine the charge transfer resistance, R_{ct}, which is a key parameter for characterizing the catalyst-electrolyte charge transfer process. The fitting parameters are listed in **Table S2**. The R_{ct} values follow an order consistent with the HER performance.

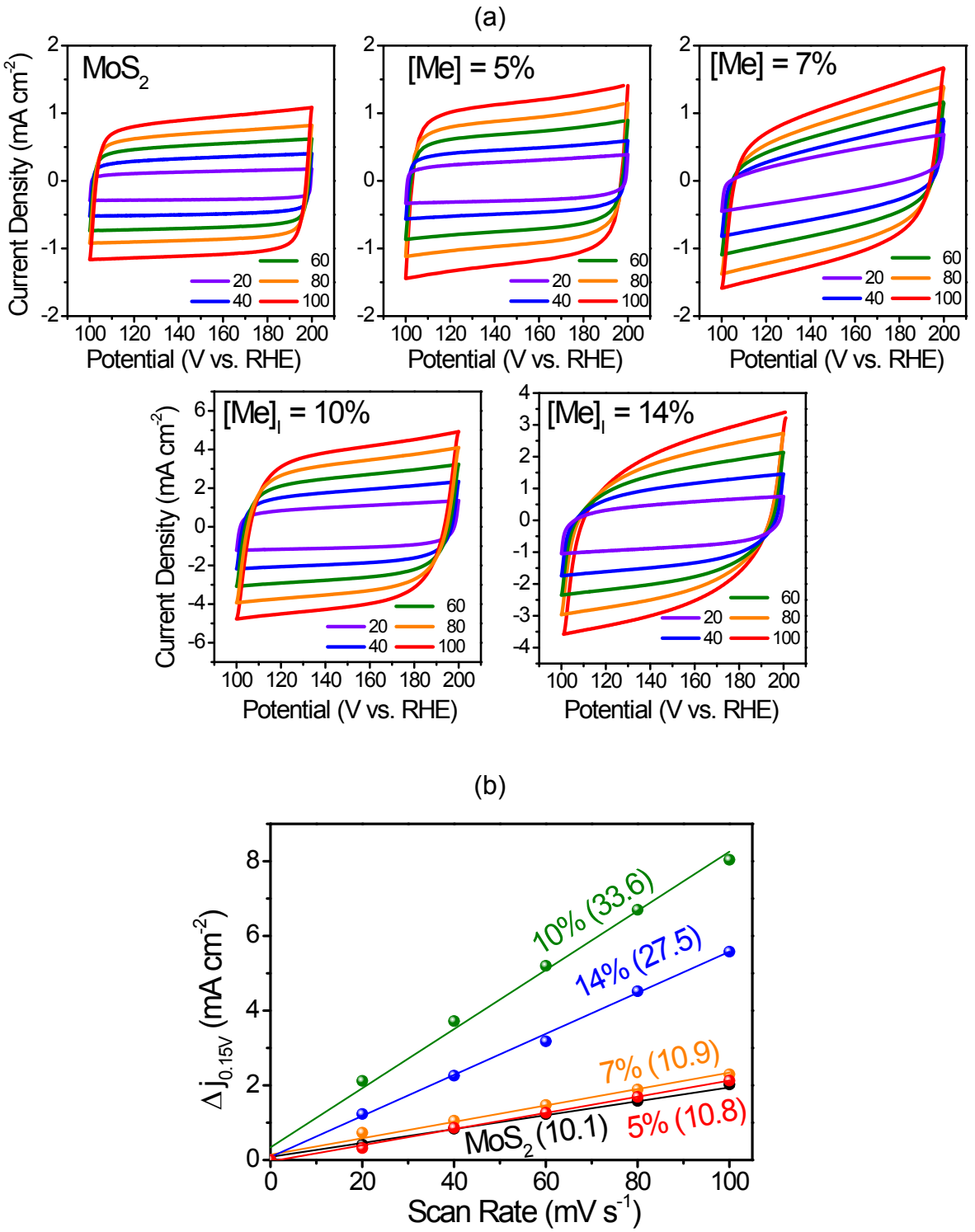

Fig. S14 (a) Cyclic voltammograms of MoS_2 and MoS_2-Me (with [Me] = 5%, 7%, 10%, and 14%), in a non-Faradaic region (0.1-0.2 V vs. RHE), at 20-100 mV s^{-1} scan rates (with a step of 20 mV s^{-1}) and in 0.5 M H_2SO_4 solution. (b) Difference (ΔJ) between the anodic charging and cathodic discharging currents measured at 0.15 V (vs. RHE) and plotted as a function of

the scan rate. The value in parenthesis represents the C_{dl}, obtained by the half of the linear slope.

Cyclic voltammograms were measured at 0.1-0.2 V, in a non-Faradaic region, using various scan rates. The double-layer capacitance (C_{dl}) was obtained as the slope (half value) of a linear fit of ΔJ vs. scan rate (20-100 mV s^{-1}), where ΔJ is the difference between the anodic charging (positive value) and cathodic discharging currents (positive value). The C_{dl} value increases with increasing [Me] until 10%, and then decrease at the higher [Me], consistently with the concentration dependence of HER performance. Therefore, the double-layer capacitance determines the HER catalytic activity of MoS_2-Me samples.

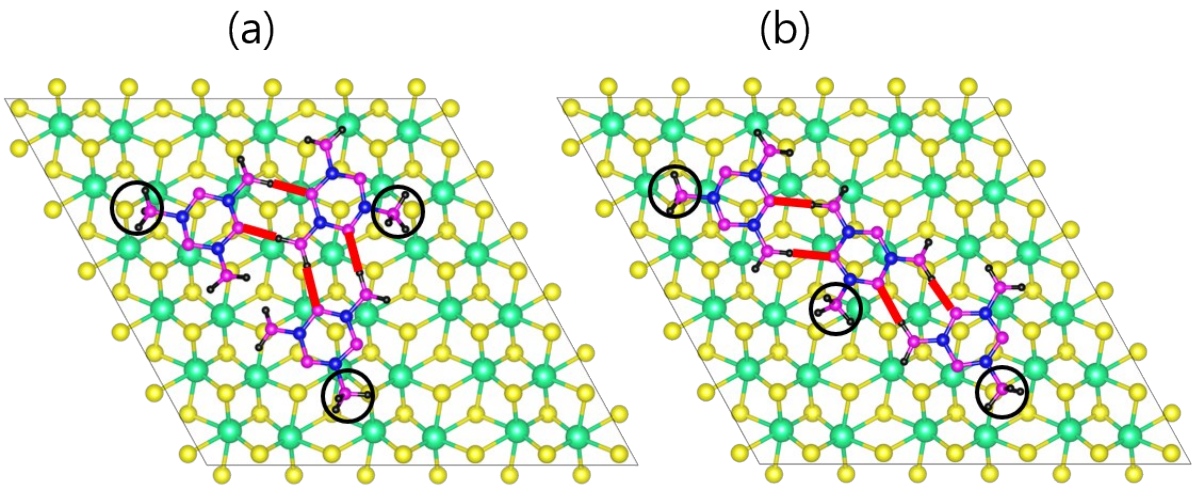

Fig. S15 Structure (ball-and-stick model) of 1T' phase (6×6) MoS_2-MeH-3 in (a) triangular (**T**) or (b) linear (**L**) configurations. Green, yellow, blue, magenta, and black balls represent the Mo, S, C, N, and H atoms, respectively. The black circle shows that one of three NH_2 groups is hydrogenated to form NH_3. The red bars represent the hydrogen bonds between adjacent MeH. The **T** configuration is more stable than the **L** configuration by 0.06 eV per MeH.

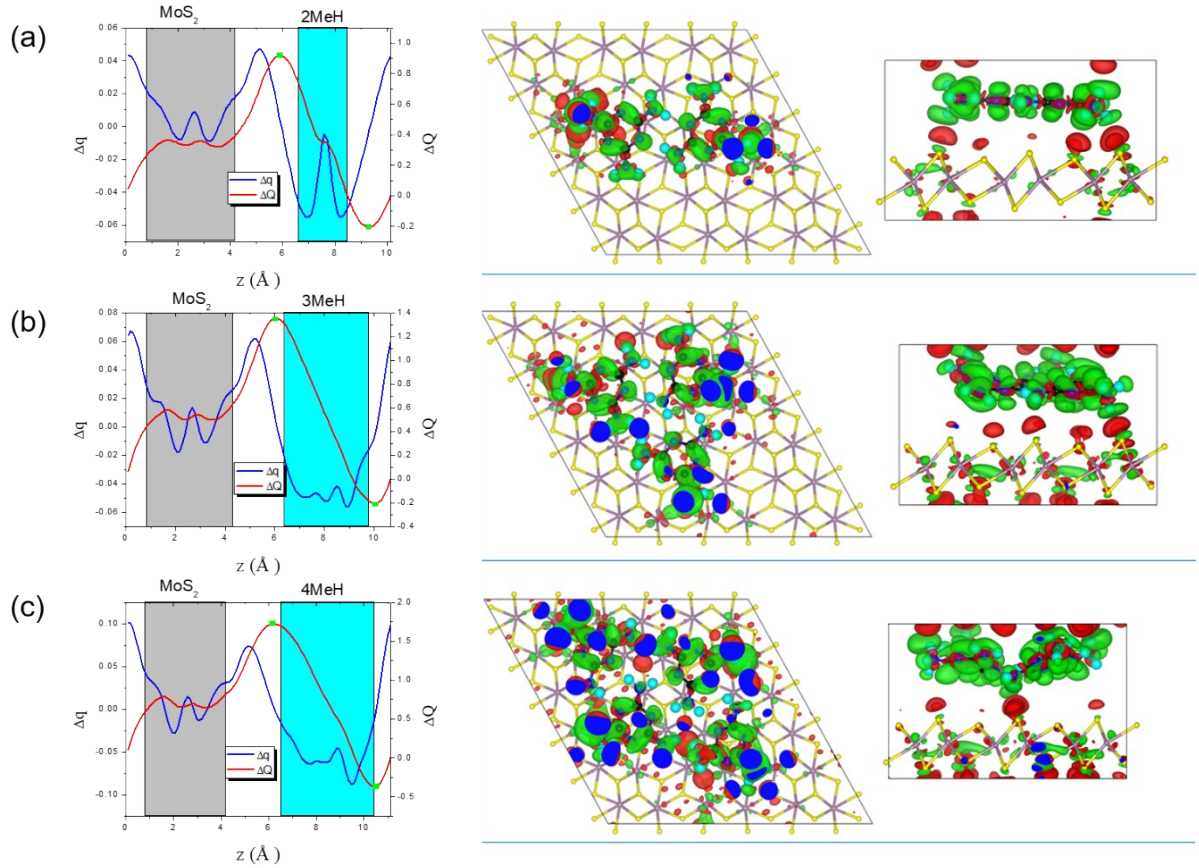

Fig. S16 Δq(z) and ΔQ(z) for (6×6)MoS_2-MeH-*n* where (a) *n* = 2, (b) *n* = 3, and (c) *n* = 4 versus z: z_{min} and z_{max} values corresponding to $Q_{min}(z)$ and $Q_{max}(z)$ are shown by filled squares (■), respectively. The differential charge density Δρ(x, y, z) contour plot: charge accumulation and depletion regions are represented by red and green colors, respectively.

Following our previous studies, the amount of the charge transfer was calculated. The change in electron density (expressed in *e* Å^{-3}) along the *c* (= *z*) axis generated by the intercalation process was defined as $\Delta\rho(z) = \rho(z)\{MoS_2\text{-MeH}\} - \rho(z)\{MoS_2\} - \rho(z)\{MeH\}$, averaged over the *xy* plane in a supercell. The total electron density change (*e*) was defined as $\Delta q(z) = \Delta\rho(z)\Delta V$, where ΔV is the volume of a fine grid, *i.e.*, $\Delta V = V_{cell}/N_c$, in which V_{cell} is the total volume of the supercell and N_c is the number of fine grids. The thickness of each MoS_2 layer was defined on the basis of the *z* coordinates of the S atoms in the upper and lower sublayers (S_L and S_U), with $z(S_L) < z(S_U)$. The thickness of MeH molecules was obtained from the minimum and maximum *z* coordinates of its atoms. The actual thickness might be larger than that obtained using this definition if the finite atomic size is taken into account. In addition, *Q*(*z*), displayed on the right vertical axis represents the accumulated excess charge in the

interval [0, z]: $Q(z)=\sum_{0}^{z'<z}\Delta q(z')$, i.e., the integration of charge difference $\Delta q(z')$ within $z' < z < c$.

The amount of charge transfer was defined as $\Delta Q = Q_{max} - Q_{min}$, where Q_{max} and Q_{min} correspond to the maximum and minimum charge values in the regions (marked by ■) adjacent to the MoS_2 layers and MeH molecules, respectively. The ΔQ was about 0.5e per MeH.

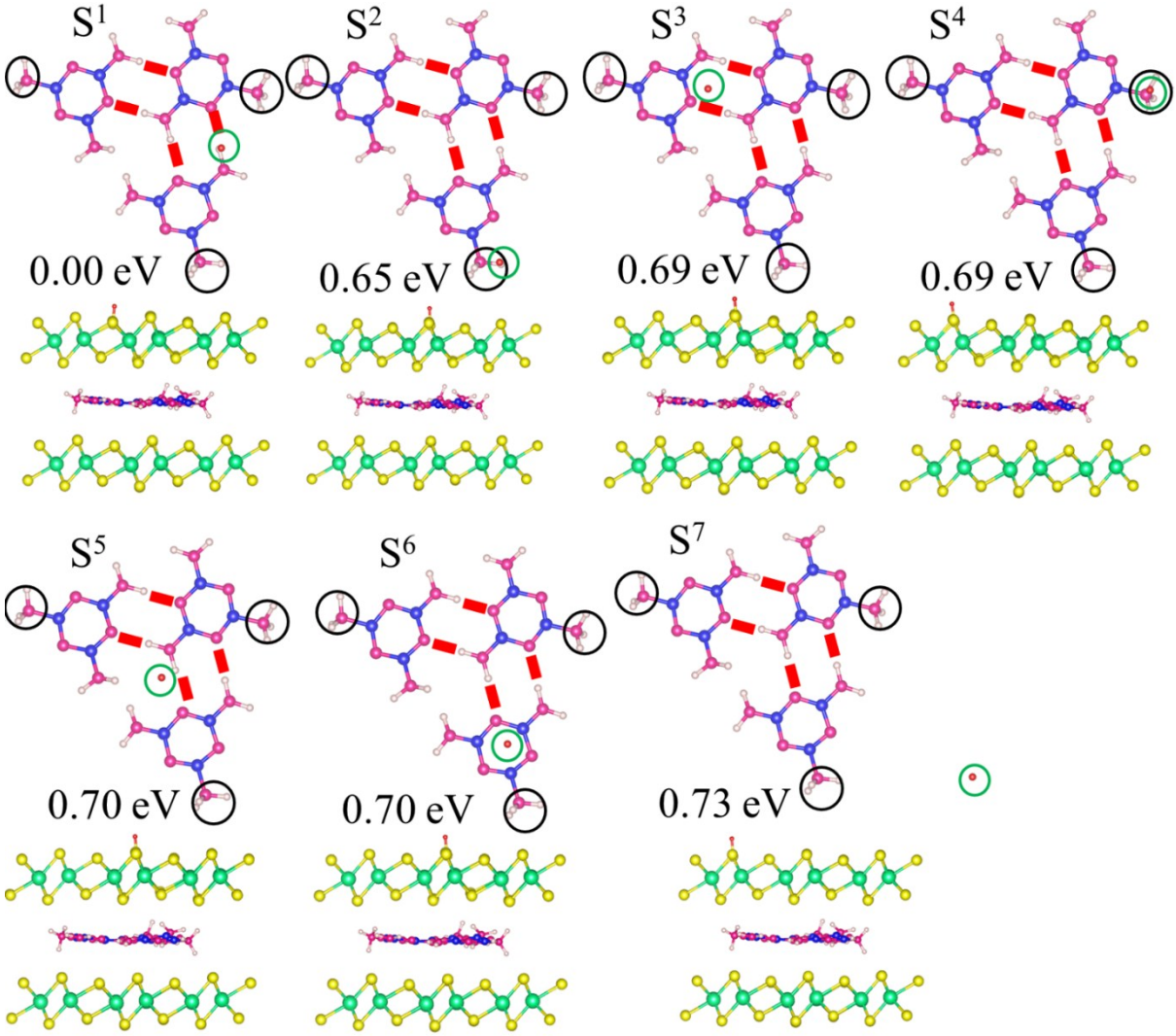

Fig. S17 Structure (ball-and-stick model) of 1T′ phase (6×6) $2MoS_2$-MeH-3 in slab geometry, showing various S adsorption sites of a H atom (red balls) in Volmer reaction. For clarity, we show top views without the MoS_2 layers, while side views are shown for the entire complex.

The relative energy (in eV) of each adsorption S site is shown with respect to that of S^1 configuration. Green, yellow, blue, magenta, and white balls represent the Mo, S, C, N, and H atoms of the complex, respectively. Green circles indicate various S adsorption sites of an H atom (red ball) considered. Black circles represent amine groups that are hydrogenated to form NH_3, and red bars represent the hydrogen bonds between adjacent MeHs. The S^1 site is the S located above the hydrogen bonded NH_2 group. S^2 site represents the S above the H of NH_3 group. S^3 is the S located above the middle of adjacent hydrogen bonds. S^4 , S^5, S^6, and S^7 denote the S above the N atom of NH_3 group, the near site of NH_2 group, the center of a triazine ring, and the site far away from the MeH, respectively. Therefore, Volmer reaction occurs in a specific site.

IV. References

S1. C. C. L. McCrory, S. Jung, I. M. Ferrer, S. M. Chatman, J. C. Peters and T. F. Jaramillo, *J. Am. Chem. Soc.*, 2015, **137**, 4347-4357.

S2. Y. Yin, J. Han, Y. Zhang, X. Zhang, P. Xu, Q. Yuan, L. Samad, X. Wang, Y. Wang, Z. Zhang, P. Zhang, X. Cao, B. Song and S. Jin, *J. Am. Chem. Soc.*, 2016, **138**, 7965-7972.

S3. D. Voiry, M. Salehi, R. Silva, T. Fujita, M. Chen, T. Asefa, V. B. Shenoy, G. Eda and M. Chhowalla, *Nano Lett.*, 2013, **13**, 6222-6227.

S4. M. A. Lukowski, A. S. Daniel, F. Meng, A. Forticaux, L. Li and S. Jin, *J. Am. Chem. Soc.*, 2013, **135**, 10274-10277.

S5. Z. Wu, C. Tang, P. Zhou, Z. Liu, Y. Xu, D. Wang and B. Fang, *J. Mater. Chem. A*, 2015, **3**, 13050-13056.

S6. D. Voiry, R. Fullon, J. Yang, C. C. C. Silva, R. Kappera, I. Bozkurt, D. Kaplan, M. J. Lagos, P. E. Batson, G. Gupta, A. D. Mohite, L. Dong, D. Er, V. B. Shenoy, T. Asefa and M. Chhowalla, *Nat. Mater.*, 2016, **15**, 1003-1009.

S7. X. Geng, W. Sun, W. Wu, B. Chen, A. Al-Hilo, M. Benamara, H. Zhu, F. Watanabe, J. Cui and T. Chen, *Nat. Commun.*, 2016, **7**, 10672.

S8. J. Zhang, J. Wu, H. Guo, W. Chen, J. Yuan, U. Martinez, G. Gupta, A. Mohite, P. M. Ajayan and J. Lou, *Adv. Mater.*, 2017, **29**, 1701955.

S9. E. E. Benson, H. Zhang, S. A. Schuman, S. U. Nanayakkara, N. D. Bronstein, S. Ferrere, J. L. Blackburn and E. M. Miller, *J. Am. Chem. Soc.*, 2018, **140**, 441-450.

S10. Z. Luo, Y. Ouyang, H. Zhang, M. Xiao, J. Ge, Z. Jiang, J. Wang, D. Tang, X. Cao, C. Liu and W. Xing, *Nat. Commun*., 2018, **9**, 2120.

S11. J. Luxa, P. Vosecký, V. Mazánek, D. Sedmidubský, M. Pumera and Z. Sofer, *ACS Catal.*, 2018, **8**, 2774-2781.

S12. C. Tan, Z, Luo, A. Chaturvedi, Y. Cai, Y. Du, Y. Gong, Y. Huang, Z. Lai, X. Zhang, L. Zheng, X. Qi, M. H. Goh, J. Wang, S. Han, X. J. Wu, L. Gu, C. Kloc and H. Zhang, *Adv. Mater*., 2018, **30**, 1705509.

S13. E. W. Hughes, *J. Am. Chem. Soc*., 1941, **63**, 1737-1752.

S14. N. Tian, Y. Zhang, X. Li, K. Xiao, X. Du, F. Dong, G. I. N. Waterhouse, T. Zhang and H. Huang, *Nano Energy* 2017, **38**, 72-81.

S15. B. Jürgens, E. Irran, J. Senker, P. Kroll, H. Müller and W. Schnick, *J. Am. Chem. Soc.* 2003, **125**, 10288-10300.

S16. D. Yang, S. J. Sandoval, W. M. R. Divigalpitiya, J. C. Irwin and R. F. Frindt, *Phys. Rev. B*, 1991, **43**, 12053-12056.

S17. H. Huang, C. Shende, A. Sengupta, F. Inscore, C. Brouillette, W. Smith and S. Farquharson, *J. Raman Spectrosc.* 2012, **43**, 701-705.

S18. Y. Fu, J. Zhu, C. Hu, X. Wu and X. Wang, *Nanoscale*, 2014, **6**, 12555-12564.

S19. W. Zhang, H. Huang, F. Li, K. Deng and X. Wang, *J. Mater. Chem. A*, 2014, **2**, 19084-19094.